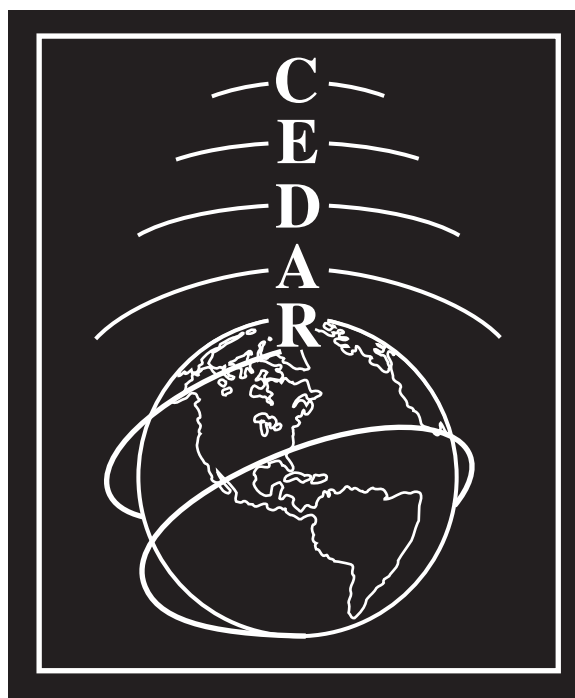


**2000 CEDAR Workshop  
NOAA/NIST  
Boulder, Colorado, USA  
June 25-30, 2000**

**Poster Sessions Booklet  
NOAA, June 27-28, 6-9 PM**



**Sponsored by HAO/NCAR, NSF, and NOAA**

# Contents

<b>1</b>	<b>Tuesday Evening 27 June 2000 Poster Session Titles, Analysis Techniques (A)</b>	<b>6</b>
1.1	A01: ISR neutral winds and collision frequencies: new insights by Heinselman, Craig . . . . .	6
1.2	A02: Triangulation of Auroral Emission Heights by Jackel, Brian J . . . . .	6
1.3	A03: Digisonde Vertical Drift Velocity Measuring Technique by (student in competition) Paznukhov, Vadym . . . . .	6
1.4	A04: Auroral Arc Referenced Convection Patterns from SuperDARN by Ruohoniemi, Michael	6
1.5	A05: Electrostatic Potential Patterns in the High Latitude Constrained by SuperDARN Measurements by Shepherd, Simon . . . . .	6
1.6	A06: The LT-UT mapping of equivalent currents. by ZAITZEV, Alexander . . . . .	7
<b>2</b>	<b>Tuesday Evening 27 June 2000 Poster Session Titles, Instruments (N)</b>	<b>8</b>
2.1	N01: Laser Induced Fluorescence Studies of the Middle Atmosphere by (student in competition) Breese, Justin . . . . .	8
2.2	N02: The Firepond Lidar at MIT Haystack Observatory by Duck, Thomas J. . . . .	8
2.3	N03: Evaluation of a Liquid Crystal Fabry-Perot for use in Lidar applications by Sipler, Dwight	8
2.4	N04: A "Fly-Eye" Mosaic Fabry-Perot for Airglow Spectroscopy by Kerr, Robert B. . . . .	8
2.5	N05: Simultaneous Multispectral Imaging of Auroral Fine Structure by Semeter, Joshua . .	9
2.6	N06: The Platteville Atmospheric Observatory by (student in competition) McQuerry, Shawn	9
2.7	N07: The Pohnpei Radar Observatory - PRO by Ecklund, Warner L. . . . .	9
2.8	N09: A Low-Cost, Remotely-Deployable Meteor Radar System for Mesosphere/Ionosphere Coupling Studies by Palo, Scott . . . . .	9
2.9	N09: Wide-beam forming using binary phase coding by Woodman, Ronald F. . . . .	10
2.10	N10: Current Performance of the TIMED Doppler Interferometer (TIDI) by Kafkalidis, Julie F. . . . .	10
2.11	N11: Solar EUV Observation from GOES: Objectives and Instrument Design by Viereck, Rodney . . . . .	10
<b>3</b>	<b>Tuesday Evening 27 June 2000 Poster Session Titles, Ionosphere and Coupling to the Magnetosphere and Neutral Atmosphere (O)</b>	<b>11</b>
3.1	O01: Intermediate Layers and Associated Vertical Ion Drifts by (student in competition) Bishop, Rebecca . . . . .	11
3.2	O02: Incoherent-Scatter Radar Studies of Metal Ion Composition in Sporadic-E Double Layers by (student in competition) Suzuki, Nobuhiro . . . . .	11
3.3	O03: A Study of the Arecibo Micrometeor Entry Kinetics in the Upper Atmosphere by (student in competition) Janches, Diego . . . . .	11
3.4	O04: Simulations and analysis of meteor trail plasma dynamics and diffusion in the ionosphere by (student in competition) Dyrud, Lars . . . . .	11
3.5	O05: Lower ionospheric collision frequencies: A comparison of radar measurements and laboratory data by Vincent, Robert A. . . . .	12
3.6	O06: In search of vibrationally excited N <sub>2</sub> effects on NmF <sub>2</sub> . by Richards, Phil . . . . .	12
3.7	O07: Equatorial electrojet irregularities investigations using a 50 MHz back-scatter radar and a digisonde: some initial results by Abdu, Mangalathayil A. . . . .	12
3.8	O08: Interferometry Investigations of Blob-like Sporadic E Plasma Irregularity Using The Chung-Li VHF Radar by Wang, Chien-Ya . . . . .	12
3.9	O09: Characterization of Equatorial Plasma Irregularities by (student in competition) Hei, Matthew A. . . . .	13
3.10	O10: Results of a Neural Network Prediction Study for Equatorial Spread-F by (student in competition) Rasmussen, Beatrice K. . . . .	13
3.11	O11: Measurements of the latitudinal distribution of TEC during Equatorial Spread-F events by Valladares, Cesar E. . . . .	13
3.12	O12: Numerical modeling of Jicamarca densities and GPS TEC values by Valladares, Cesar E.	13

3.13	O13: Interhemispheric Flows in the Equatorial Topside Ionosphere by (student NOT in competition) Venkatraman, Sarita . . . . .	14
3.14	O14: Comparison of ionospheric parameters derived from airglow observations and incoherent scatter radar measurements by (student in competition) Makela, Jonathan J . . . . .	14
3.15	O15: INHOMOGENEOUS STRUCTURE OF IONOSPHERE OVER ARECIBO by (student in competition) Zhou, Qina . . . . .	14
3.16	O17: Title: Ionospheric Tomography with the Global Positioning System by Tsai, Lung-Chih	14
3.17	O18: The traveling ionospheric disturbances observed by GPS receivers at mid-latitudes by Saito, Akinori . . . . .	15
3.18	O19: Gravity Wave Signatures in the Ionosphere of Jupiter. by (student in competition) Matcheva, Katia . . . . .	15
3.19	O20: Vibrational distributions of the N <sub>2</sub> <sup>+</sup> (A) and N <sub>2</sub> <sup>+</sup> (B) states in the terrestrial midlatitude and auroral ionospheres by Fox, Jane L. . . . .	15
3.20	O21: Global Conductances from AMIE using POLAR UVI images by CROWLEY, GEOFF	15
3.21	O22: Performance of the Weimer Ionospheric Convection Model Model with Satellite Data for Space Weather Applications by Hairston, Marc . . . . .	16
3.22	O23: Convection Electric Field Products at the JHU/APL SuperDARN Web Site by Greenwald, Raymond . . . . .	16
3.23	O24: The Polar Ionosphere under conditions of Northward IMF: Numerical Modeling and comparison with data by (student in competition) Kombiyil, Raj . . . . .	16
3.24	O25: Near-simultaneous POLAR and DMSP Measurements of Topside Ionospheric Field-aligned Flows at High Latitudes by (student in competition) Zeng, Wen . . . . .	16
3.25	O26: Whistler-mode Wave Injection Experiments in the Plasmasphere with a Radio Sounder by (student in competition) Chen, Xiangdong . . . . .	17
3.26	O27: The Role of Wave-Particle Interactions on Ionosphere-Magnetosphere Coupling by Barakat, Abdallah . . . . .	17
3.27	O28: A Statistical Survey of the Effects of Solar Wind Structures on the Ionosphere and Magnetosphere by Knipp, Delores . . . . .	17
3.28	O29: A fully coupled global MHD model of the magnetosphere and ionosphere by schoendorf, jackie . . . . .	18
<b>4</b>	<b>Wednesday Evening 28 June 2000 Poster Session Titles, Mesopause Region and Below (M)</b>	<b>19</b>
4.1	M01: Long-term variations of atmospheric waves observed with meteor and MF radars in Indonesia by Tsuda, Toshitaka . . . . .	19
4.2	M02: Initial Observations of Mesospheric Winds Using IDI Radar Measurements at the Bear Lake Observatory by studentno; changed to studentyes (meh 6/12/00) Fish, Chad . . . . .	19
4.3	M3: Observations of PMSE Using Coherent Radar Imaging: Direct Evidence of Wave Steepening by (student in competition) Yu, Tian-You . . . . .	19
4.4	M04: The Photolysis of Sodium Compounds in the Upper Atmosphere by (student in competition) Self, Daniel Emitt . . . . .	19
4.5	M05: Analysis of Na Temperature Lidar Measurements: Calculation of Stability of the Mesopause Region by (student NOT in competition) Madine, Sean . . . . .	20
4.6	M06: Mesospheric Stability and Temperatures Over Utah and Ontario by (student in competition) Nelson, Karen L . . . . .	20
4.7	M07: Lidar Observations of Middle Atmosphere Temperature and Fe Density During the 1999 Airborne Arctic Campaign by (student in competition) Pan, Weilin . . . . .	20
4.8	M09: Rayleigh Lidar Studies of the Arctic Middle Atmosphere by (student in competition) Cutler, Laura J. . . . .	20
4.9	M09: Climatology from Atmospheric Lidar Observatory USU/CASS by (student in competition) Herron, Joshua . . . . .	20
4.10	M10: Mesospheric Temperatures Probed by Simultaneous Measurement of OH and O <sub>2</sub> in the Nightglow by Cosby, Philip C. . . . .	21

4.11	M11: Resolving Ambiguities in Gravity Wave Propagation Directions Inherent in Satellite Observations: A Simulation Study by Brown, Jason S. . . . .	21
4.12	M12: The Numerical Simulation of Gravity Wave Packets and Their Effects on the OI 5577 Airglow by Hickey, Michael . . . . .	21
4.13	M13: Effects of Mean Winds on Gravity Wave-Driven O2 Atmospheric Airglow Fluctuations by (student NOT in competition) Hammett, Robert . . . . .	21
4.14	M14: Relation of Intensity Perturbation and Vertical Wind Velocity of Acoustic Gravity Wave by (student in competition) Hsia, Justin . . . . .	22
4.15	M15: Investigation of Gravity Waves Using Starfire Data by Huang, Tai-Yin . . . . .	22
4.16	M16: Directional Dependence of Gravity Wave Propagation Over Fort Collins Colorado by (student in competition) Jorgensen, Arlynda . . . . .	22
4.17	M17: Characteristic of Atmospheric Gravity Waves observed during the WAVE2000 Campaign in Japan by (student in competition) Onishi, Hisanaga . . . . .	22
4.18	M18: Observations of High Frequency Gravity Wave Spectra in the Middle Upper Stratosphere by (student in competition) Russell, Albert . . . . .	22
4.19	M19: Automation and Animation Techniques for Investigation of Gravity Waves in the Infrared Airglow by (student NOT in competition) Krueger, Todd M. . . . .	23
4.20	M20: Simulation of 3-day Kelvin wave influence on Greenline, O2 Atmospheric, and OH Meinel band emissions in the MLT region. by (student in competition) Lichstein, Gilbert S. . . . .	23
4.21	M21: Dynamical processes related to the atomic oxygen springtime transition by Liu, Han-Li . . . . .	23
4.22	M22: Uranus: Gravity waves, the momentum budget, and adiabatic cooling. by Young, Leslie A. . . . .	23
4.23	M23: A Mechanistic Wave-Mean Flow Interaction Model - First Results by Meyer, Christian . . . . .	24
4.24	M24: Intradiurnal Oscillations in the Mesosphere and Lower Thermosphere by (student in competition) Sharma, Niranjana . . . . .	24
4.25	M25: Migrating and Nonmigrating Semidiurnal Tide Components From Combined Space-based and Ground-based Measurements by (student in competition) Cierpik, Kim . . . . .	24
4.26	M26: TIME-GCM simulations of the diurnal variation of lower thermospheric nitric oxide observed by HALOE by Marsh, Dan . . . . .	24
4.27	M27: Nitrous Oxide(N2O) production in sprites by (student in competition) Moudry, Dana . . . . .	25
4.28	M28: Statistical Parameters of Lightning in Sprite-Associated Storms. by (student in competition) So Sabbas, Fernanda T. . . . .	25
4.29	M29: Estimation of the Energies of Electrons Inducing Elves Observed above Japan in Winter by (student in competition) Miyasato, Rina . . . . .	25
4.30	M30: A Study of 19.5 GHz Brightness Temperature over Taiwan Area by (student NOT in competition) Shih, Shun-Peng . . . . .	25
4.31	M31: Anomalous Behavior of Precipitation Doppler Spectrum Associated With Strong Vertical Air Motion by (student NOT in competition) Su, Ching-Lun . . . . .	26
<b>5</b>	<b>Tuesday Evening 27 June 2000 Poster Session Titles, Thermosphere and Regions Aloft (T)</b>	<b>27</b>
5.1	T01: Estimates of Terdiurnal Oscillations at Sondre Stromfjord by Azeem, Irfan . . . . .	27
5.2	T02: COMPARISON OF THE AURORAL E REGION NEUTRAL WINDS DERIVED BY THE EISCAT RADAR AND PREDICTED BY NCAR TIME-GCM. by Nozawa, Satonori . . . . .	27
5.3	T03: Neutral winds in the lower thermosphere observed by WINDII during the April 4-5th, 1993 and February 1994 storms by Zhang, Shengpan . . . . .	27
5.4	T04: Thermospheric Vertical Winds at the Auroral Oval/Polar Cap Boundary by (student in competition) Krynicki, Matthew P. . . . .	27
5.5	T05: Verifying Thermospheric Composition Effects due to Vertical Winds by (student in competition) Krynicki, Matthew P. . . . .	28
5.6	T06: SWIFT - ITCI: Space Weather Ionospheric Forecasting Tools an Ionosonde Thermospheric Composition Index by Wright, John William . . . . .	28

5.7	T07: Fabry-Perot Observations of the Hydrogen Geocorona by (student in competition)	
	Mierkiewicz, Edwin, J. . . . .	28
5.8	T08: Determination of geocoronal H-alpha intensities and upper atmospheric hydrogen densities from WHAM FP observations. by Nossal, Susan . . . . .	28

## 1 Tuesday Evening 27 June 2000 Poster Session Titles, Analysis Techniques (A)

### 1.1 A01: ISR neutral winds and collision frequencies: new insights by Heinselman, Craig

**Authors:** Craig Heinselman Jeffrey Thayer

**Abstract:** ISR measurements of E-region neutral winds have a natural coordinate system based on the direction of the perpendicular current vector. We exploit this coordinate system to gain insight into the relationship between collision frequency and wind estimates.

### 1.2 A02: Triangulation of Auroral Emission Heights by Jackel, Brian J

**Authors:** Brian J Jackel Eric F Donovan Leroy L Cogger

**Abstract:** Ten years of meridian scanning photometer data from the CANOPUS array are used in a study of auroral emission heights. Triangulation between adjacent sites provides information about the location and altitude of red-line, green-line, and N2+ emissions. Inferred heights are well correlated with characteristic energy estimated from standard spectroscopic ratios.

### 1.3 A03: Digisonde Vertical Drift Velocity Measuring Technique by (student in competition) Paznukhov, Vadym

**Authors:** V.V. Paznukhov, G.S. Sales, and B.W. Reinisch

**Abstract:** This research was aimed at developing a new technique for measuring vertical plasma motion. Using a Digisonde, it is possible to derive an apparent velocity from the movement of plasma isodensity contours. However, this does not represent the true plasma drift speed since chemical processes also contribute to the changing plasma density contours. We solve the continuity equation in order to separate the plasma drift from the chemistry. The comparison between vertical drift velocities calculated by this technique and measured with the collocated incoherent scatter radar shows good correspondence.

### 1.4 A04: Auroral Arc Referenced Convection Patterns from SuperDARN by Ruohoniemi, Michael

**Authors:** J. M. Ruohoniemi, R. A. Greenwald, S. G. Shepherd, and K. Liou

**Abstract:** A significant improvement has been made to the standard APL technique of fitting ionospheric convection velocity data to produce maps of the plasma convection in the high-latitude. Velocity data are mapped into new coordinates referenced to auroral arc boundaries determined from UVI data on the POLAR spacecraft. The new patterns produced with this technique preserve smaller-scale features that are otherwise obscured.

### 1.5 A05: Electrostatic Potential Patterns in the High Latitude Constrained by SuperDARN Measurements by Shepherd, Simon

**Authors:** S. G. Shepherd and J. M. Ruohoniemi

**Abstract:** The recent addition of two radars to the northern hemisphere component of SuperDARN has significantly extended the area in the high-latitude where measurements of convecting plasma are made. Periods are now common during which measurements, available over nearly 3/4 of the high-latitude region, adequately constrain maps of the electrostatic potential produced by an established fitting technique. During such periods the solution for the global potential pattern is insensitive to the choice of statistical model data used to constrain the fitting.

## 1.6 A06: The LT-UT mapping of equivalent currents. by ZAITZEV, Alexander

**Authors:** A.N.Zaitzev, V.I.Odintsov, IZMIRAN, Troitsk near Moscow, 142190, RUSSIA

**Abstract:** LT-UT mapping of the H component of ground magnetometer deviations was introduced by Zaitzev and Bostrom in 1971 (Plan. Space Sci., 1971, v.19, no.5, pp.643-649) and has become a standard tool in searching for equivalent currents. First of all it was adopted to analyse the spatial-temporal distribution of polar electrojets as inferred from AE-index stations. On the LT-UT maps of the deviation of the H component based on the mean hourly values of the 12 AE stations for the CDAW-1 interval (5-10 March 1970), we display the planetary peculiarities in the development of the auroral electrojets. There are two types of currents under LT or/and UT control, the position of the maxima in the electrojets, overlapping of the electrojets, and the dependence of the Harang discontinuity on UT. With detailed maps based on 6-min values we display small-scale features in the space and time development of the electrojets. The gaps in the network of AE-stations are the main limitation in the mapping of polar currents. LT-UT mapping can also be used for the analysis of the Dst variation. For this purpose we use the latitudinal chain of stations: San Juan, M'Bour, Binza, Tbilisi, Tashkent, Munitinlupa, Kakioka, Guam, Honolulu, Tucson. The data from these stations during the magnetic storm of 5-10 March 1970 was used for the LT-UT mapping of the ring current development. The global features of the ring current were obtained including the asymmetric development and the possible connection with the polar disturbances. The prospects of using LT-UT mapping to monitor space weather is also discussed. LT-UT maps can be produced in real-time if the data are available in real time via the Internet.

## 2 Tuesday Evening 27 June 2000 Poster Session Titles, Instruments (N)

### 2.1 N01: Laser Induced Fluorescence Studies of the Middle Atmosphere by (student in competition) Breese, Justin

**Authors:** Justin Breese, Keith J. Nowicki, Richard L. Collins, Laura J. Cutler

**Abstract:** Recently a new excimer pumped dye laser was installed at the Poker Flat research range for use in a resonance lidar system. For the past year this system has been undergoing characterization and testing using sodium. The higher speed and beam quality of the new system has allowed new measurements to be made during this time and particularly during the Leonids meteor shower. Upon completion of this testing process the lidar system will be used to make temperature measurements of the mesosphere using atomic iron.

### 2.2 N02: The Firepond Lidar at MIT Haystack Observatory by Duck, Thomas J.

**Authors:** Thomas J. Duck, Dwight P. Sipler, Joseph E. Salah, John W. Meriwether

**Abstract:** A new lidar for atmospheric research is operational at the Firepond Optical Facility of MIT Haystack Observatory. The lidar currently measures temperatures between 25 and 95 km in altitude at night and up to 65km during the day. We are enhancing the lidar to extend the daytime measurements to higher altitudes and also to allow spectroscopic measurements of winds and temperatures. The lidar will be used for studies of mesospheric temperature inversions and gravity wave / mean flow interactions.

### 2.3 N03: Evaluation of a Liquid Crystal Fabry-Perot for use in Lidar applications by Sipler, Dwight

**Authors:** Dwight Sipler, Thomas Duck: MIT Haystack Observatory

**Abstract:** A liquid crystal Fabry-Perot interferometer is a relatively new optical device which has some advantages over the conventional piezoelectric or pressure tuned interferometers. Being electrically tunable, the device can be easily and rapidly tuned by computer control. Since we have an application for this device in a Doppler lidar application, it was necessary to evaluate the stability and repeatability of the tuning. Using a frequency stabilized HeNe laser, we found the device to be stable enough to use for Doppler measurements to within the precision of the measurement, equivalent to about 10 m/s.

### 2.4 N04: A "Fly-Eye" Mosaic Fabry-Perot for Airglow Spectroscopy by Kerr, Robert B.

**Authors:** R. B. Kerr J. Noto B.M. McCormack

**Abstract:** The luminosity of the Fabry-Perot Interferometer has been limited by the practical limit to which glass substrates can be ground to 1/100th wave or better and matched in an etalon. Currently that size limit is around 8 inches. By constructing a mosaic of seven 80mm hexagonal etalons, (effective clear aperture of 350 square centimeters), Scientific Solutions Inc eliminates this classical Fabry-Perot aperture limit. The key to spectral coordination is the use of liquid -crystal as the index-changing medium within the etalon gap. A spectral resolution of 2.4 pm is achieved using a 4mm gap in each of the component etalons. The total field of view is 0.11 degrees.

## 2.5 N05: Simultaneous Multispectral Imaging of Auroral Fine Structure by Semeter, Joshua

**Authors:** Joshua Semeter, Richard Doe, Michael Ertl, Gerhard Haerendel

**Abstract:** The distribution of optical energy in the auroral spectrum is sensitive to the energy and temperature of the incident particle population, and to ionospheric composition. Photometric measurements of atomic oxygen and molecular nitrogen emissions in the magnetic zenith have been used to estimate characteristic energy, energy flux, and composition scale factors. With respect to such calculations the auroral spectrum can be considered redundant; the spectral detail afforded by dispersion-based instruments is not required. Spectrographs and photometers also do not provide the spatial context required for the proper interpretation of measured precipitation with respect to auroral forms. Auroral imaging is the only diagnostic providing an instantaneous projection of magnetospheric electrodynamics, and should be exploited accordingly. Simultaneous access to the spatial information of cameras, and the spectral dimensions of photometers, provides a unique window into MI coupling in the auroral zone. This was the motivation for the Simultaneous-sampling Multispectral Imager (SMI). The SMI is a fast narrow-field camera designed to image four selected wavelengths onto a single detector simultaneously. This poster presents initial results from a campaign at Sondrestrom in March, 2000, involving measurements of auroral structures by the SMI, the all-sky camera, a 4-channel photometer, and the incoherent scatter radar.

## 2.6 N06: The Platteville Atmospheric Observatory by (student in competition) McQuerry, Shawn

**Authors:** S.McQuerry, S.Avery, J.Avery, D.Thorsen, E.Lau, S.Palo, R.Schafer, P.Johnston, R.Strauch, M.J.Post, A.Manson, C.Meek

**Abstract:** Since its founding in 1966, the Platteville Atmospheric Observatory has been at the forefront of atmospheric science. The observatory's purpose has broadened beyond its original use for ionospheric heating, by housing instruments including wind profilers, a MF radar, meteor radars, and hydrology instrumentation. In 1997, a Major Research Instrument Grant was awarded by the NSF, which has facilitated major upgrades, renovations and the installation of new instrumentation.

## 2.7 N07: The Pohnpei Radar Observatory - PRO by Ecklund, Warner L.

**Authors:** Warner L. Ecklund Roland T. Tsunoda

**Abstract:** This poster describes the Pohnpei Radar Observatory located on the island of Pohnpei in the Federated States of Micronesia (6.96 degrees N, 158.19 degrees E) on the magnetic equator. This site was originally installed by NOAA with NSF support to observe the lower atmospheric winds. In 1998 SRI International with CEDAR support began making continuous observations of the E-region, F-region and the important 150 km echoes. Examples of some of the types of data obtained are presented in this poster.

## 2.8 N09: A Low-Cost, Remotely-Deployable Meteor Radar System for Mesosphere/Ionosphere Coupling Studies by Palo, Scott

**Authors:** S.E. Palo, N.A. Makarov, J.M. Forbes, W.L. Ecklund, Yu.I. Portnyagin and B. Petrov

**Abstract:** The University of Colorado in cooperation with the Institute for Experimental Meteorology in Obninsk Russia have developed a portable, low-cost HF (30 MHz) meteor radar for studying large scale dynamical features in the mesosphere and lower-thermosphere. This system, called Cobra-1, operates without height resolution and is currently operational in Platteville Colorado (40N), Obninsk Russia (55N) and Dixon Island Russia (74N). An upgrade to Cobra-2, with height ranging, is planned for the near future. Our system and recent results will be described.

## 2.9 N09: Wide-beam forming using binary phase coding by Woodman, Ronald F.

**Authors:** Ronald F. Woodman Jorge L. Chau

**Abstract:** We introduce the first antenna "compression" scheme for coherent radars. The idea is to transmit with a large array of coded antennas at full power, and later synthesize by linear superposition and proper phasing (decoding), a small transmitting antenna, similar to a single antenna element of the array. This approach allow the use of all the available power in phased array systems where either high power transmitters cannot be used with small antennas, or the transmitted power is distributed among the antenna elements.

## 2.10 N10: Current Performance of the TIMED Doppler Interferometer (TIDI) by Kafkalidis, Julie F.

**Authors:** Julie F. Kafkalidis, Timothy L. Killeen(1), Wilbert R. Skinner, Charles J. Edmonson, Rick J. Niciejewski, Heinz J. Grassl, David A. Gell, Peter E. Hansen, and Jon D. Harvey Space Physics Research Laboratory, University of Michigan (1) also: National Center for Atmospheric Research

**Abstract:** This paper summarizes the TIDI instrument performance as installed on the TIMED spacecraft, now awaiting launch in early 2001. TIDI will measure winds, temperatures and minor constituent densities in the 60-300 km altitude range by resolving line shapes and Doppler shifts of emission lines in the 550-900 nm spectral region. The TIDI Profiler uses a single-etalon Fabry Perot Interferometer (FPI), Circle-to- Line-Interferometer Optic (CLIO), and CCD detector. Key measures of optical performance, and the resulting expected sensitivity to terrestrial airglow emissions, are reported.

## 2.11 N11: Solar EUV Observation from GOES: Objectives and Instrument Design by Viereck, Rodney

**Authors:** Rodney Viereck

**Abstract:** Most thermosphere/ionosphere models use F10.7 as the solar driver. For many applications, this is sufficient but F10.7 is only a proxy and does not represent the true solar input critical to the upper atmosphere. To address this problem, NOAA will put EUV sensors on each of the GOES satellites. The motivation for flying these instruments will be discussed. Details of the instrument design and measurement timeline will be presented.

### 3 Tuesday Evening 27 June 2000 Poster Session Titles, Ionosphere and Coupling to the Magnetosphere and Neutral Atmosphere (O)

#### 3.1 O01: Intermediate Layers and Associated Vertical Ion Drifts by (student in competition) Bishop, Rebecca

**Authors:** R.L. Bishop and G. D. Earle

**Abstract:** Intermediate or descending plasma layers form on the bottom- side of the F peak and slowly descend to altitudes near 110 km where they can remain for several hours. In the spring of 1998, Arecibo observed intermediate layers on 33 out of 35 nights of operation. Using density data from these observations in conjunction with the continuity equation, we calculate the vertical ion drifts that are consistent with variations observed in the layer motion. These drifts can be related to meridional/zonal neutral wind fields in the E region.

#### 3.2 O02: Incoherent-Scatter Radar Studies of Metal Ion Composition in Sporadic-E Double Layers by (student in competition) Suzuki, Nobuhiro

**Authors:** Nobuhiro Suzuki Brenton J. Watkins

**Abstract:** The incoherent-scatter radar at Sondrestrom, Greenland has been operated in a high-resolution mode to map thin sporadic-E metal ion layers. We report on studies of radar spectral data to estimate the mean ion mass within sporadic-E layers, in particular double layers where two parallel layers are stacked vertically with separations of about 2-10 km. Our objective is to determine the role and extent of lighter metal ions (eg Ca<sup>+</sup>, Mg<sup>+</sup>) in forming sporadic-E structures. The lighter metal layers should be reside just below the heavier layers which are mainly composed of Fe<sup>+</sup>.

#### 3.3 O03: A Study of the Arecibo Micrometeor Entry Kinetics in the Upper Atmosphere by (student in competition) Janches, Diego

**Authors:** Diego Janches John D. Mathews David D. Meisel

**Abstract:** We present details of the entry kinetics of micrometeors in the upper atmosphere derived from velocity/deceleration results found using the Arecibo Observatory 430 MHz Radar (AO). These results are obtained utilizing a Doppler technique that allows very precise determination of the instantaneous meteor velocity directly from the meteor head-echo. With the velocity, the deceleration, the assumption of a spherical shape, and a mean micrometeoroid mass density we have obtained estimates of in-atmosphere particle sizes. An estimation of meteoric mass flux into the upper atmosphere is reliably drawn. The meteor energy loss is also calculated providing clues regarding the physical processes that these particles undergo during the time they are seen by the radar.

#### 3.4 O04: Simulations and analysis of meteor trail plasma dynamics and diffusion in the ionosphere by (student in competition) Dyrud, Lars

**Authors:** L P Dyrud, M M Oppenheim, G Vetoulis, A F vom Endt

**Abstract:** Meteor trails of increased ionization created from dust to sand size grains are frequently observed at E-region altitudes in the ionosphere. We present computer simulations and analyses of meteor trails at a range of altitudes and angles with respect to the geomagnetic field and a background electric field. We find that a gradient-drift type instability forms on the edges of the trails and develops into turbulence in  $\tilde{1}$ -5 ms. This instability also drives an anomalous perpendicular diffusion that increases with trail altitude and density gradient, and may exceed the theoretical diffusion by an order of magnitude.

### 3.5 O05: Lower ionospheric collision frequencies: A comparison of radar measurements and laboratory data by Vincent, Robert A.

**Authors:** R. A. Vincent, R. Vuthaluru, D. A. Holdsworth I. M. Reid, W. G. Elford and M. T. Elford

**Abstract:** Electron densities and collision frequencies in the 60-100 km height range are measured using differential absorption techniques with the 1-km Buckland Park array located near Adelaide, Australia. The observed collision frequencies show significant differences from values calculated using laboratory-measured molecular cross-sections and observed atmospheric pressures. The discrepancy is resolved if new laboratory measurements of N<sub>2</sub>, O<sub>2</sub>, and O collision cross-sections for momentum transfer are incorporated. The effect is to significantly increase collision frequencies over previously used values, with implications for calculations of ionospheric current strengths.

### 3.6 O06: In search of vibrationally excited N<sub>2</sub> effects on NmF<sub>2</sub>. by Richards, Phil

**Authors:** Phil G. Richards S. Daniel Daugherty

**Abstract:** Several studies have predicted up to a factor of 2 reduction in NmF<sub>2</sub> as a result of significant amounts of vibrationally excited N<sub>2</sub> in summer at solar maximum. Vibrationally excited N<sub>2</sub> reacts much faster with O<sup>+</sup> than does ground state N<sub>2</sub>. To study this problem, we compare the FLIP model predictions of NmF<sub>2</sub>, with and without vibrationally excited N<sub>2</sub>, against measurements at a selection of globally distributed ionosonde stations over the solar cycle from 1976-80.

### 3.7 O07: Equatorial electrojet irregularities investigations using a 50 MHz back-scatter radar and a digisonde: some initial results by Abdu, Mangalathayil A.

**Authors:** M. A. Abdu, C. M. Denardini, J. H. A. Sobral, I. S. Batista, P. Muralikrishna, R. R. de Paula

**Abstract:** A new 50 MHz coherent back-scatter radar has recently become operational at the Equatorial Space Observatory of INPE at So Luis (2.33 S, 44.2W, dip: -0.5), in Brazil. Preliminary results from a 10-day campaign in December 1999 involving this radar and a digisonde are presented in this paper. The RTI maps of electrojet irregularities show short period (5 minutes or larger) fluctuations and significant day-to-day variabilities. A notable characteristic is the midday descent in the altitude of the RTI pattern that resembles the diurnal pattern of the base height of the q-type sporadic E layer observed by the digisonde and that of the well known 150 km echoes observed over Jicamarca and Pompei.

### 3.8 O08: Interferometry Investigations of Blob-like Sporadic E Plasma Irregularity Using The Chung-Li VHF Radar by Wang, Chien-Ya

**Authors:** Chien-Ya Wang Yen-Hsyang Chu

**Abstract:**

Radar echoes from 3-meter plasma irregularities of ionospheric sporadic E (Es) layer are analyzed and investigated in this article by using the Chung-Li VHF radar. The interferometry result indicates that the Es irregularities extending from about 109 to 122 km are extremely aspect sensitive with enormously narrow aspect angle of 0.25°. After reconstructing the 3-dimensional structure of the Es echoes, we find that the object responsible for the radar returns is an isolated and solid blob-like plasma irregularity with elliptical cross section. The averaged lengths of the major and minor axes of the cross section are, respectively, 8.7 and 6.4 km, in which the major axis is basically parallel to the north-south direction and minor axis lies in the east-west direction. A comparison between the trace drift velocity  $V_a$  deduced from the bulk displacement of the plasma structure projected on three mutually orthogonal planes and the true drift velocity  $V_t$  estimated from the least squares fit is also made.

### 3.9 O09: Characterization of Equatorial Plasma Irregularities by (student in competition) Hei, Matthew A.

**Authors:** Matthew A. Hei (first author) Roderick A. Heelis (advisor)

**Abstract:** Equatorial plasma irregularities (bubbles) are a complex and morphologically diverse phenomenon; they have been observed to have a wide variety of scale sizes, packing densities, density depletion magnitudes, and edge gradients. Furthermore, depletions can at times appear to be superimposed on large-scale background modulations, while at other times they may appear as individual density depletions. The work presented here is used to determine characteristic bubble scale sizes, scale size distribution as a function of local time, and the relationships between spatial size and depletion magnitude.

### 3.10 O10: Results of a Neural Network Prediction Study for Equatorial Spread-F by (student in competition) Rasmussen, Beatrice K.

**Authors:** Beatrice K. Rasmussen Greg Earle

**Abstract:** Neural network algorithms have been used in conjunction with DMSF satellite data in a study of Equatorial Spread-F (ESF) over Ascension Island. DMSF satellite data were processed and provided as inputs to the networks to determine if ESF prediction was possible. Results of the neural network studies suggest that the pre-sunset topside ionospheric densities, temperatures, and velocities are not significantly preconditioned for post-sunset ESF development. A possible explanation is presented as to the reliability of this approach as a predictor of ESF.

### 3.11 O11: Measurements of the latitudinal distribution of TEC during Equatorial Spread-F events by Valladares, Cesar E.

**Authors:**

C. E. Valladares, S. Basu, K. Groves, M.P. Hagan, D. Hysell, A. J. Mazzala Jr., and R. Sheehan

**Abstract:** This paper combines three data sets in an attempt to determine the general characteristics of the latitudinal distribution of TEC when equatorial spread-F (ESF) plumes grow and when they are absent. To determine the date and times when ESF plumes (or bubbles) have developed, we have used the range-time intensity plots of coherent echoes collected by the Julia radar in 1998. We have also employed records of scintillations from two sites (Ancon and Antofagasta) displaced in latitude by 12deg. The last data set comprises latitudinal profiles of TEC constructed from measurements from several GPS receivers located at South America, also for year 1998.

### 3.12 O12: Numerical modeling of Jicamarca densities and GPS TEC values by Valladares, Cesar E.

**Authors:** C. E. Valladares, and R. F. Woodman

**Abstract:** This paper presents the analysis of data collected by the Jicamarca radar and the numerical modeling of the densities measured at this site. The combined analysis-modeling has been performed for three data periods (November 23-25, 1992, February 1-4, 1995, and May 1-5, 1995). Density profiles were obtained from power profiles and normalized by the peak density measured by the local digisonde. Profiles of vertical drifts have been also extracted from the Jicamarca phase measurements of the incoherent scatter signal. We have used the Jicamarca vertical drifts to run the low-latitude part of the global theoretical ionospheric model (GTIM). The model runs have been conducted first using drifts values averaged in altitude and then using the drift profiles. In general the agreement between the modeled and the measured peak density is very good. A better agreement is achieved using drift profiles instead of the averaged values. We also present TEC values measured from a new GPS station located at Iquitos, Peru (Lat. = 03deg; 46.0 S, Long = 73deg; 16.5 W, Alt = 135.0 m). Data collected from this station reflect the typical diurnal pattern of TEC variations seen at low-latitude stations. TEC depletions were observed on some of

the nights. The GTIM model also provides the densities at latitudes between +20deg; and -20deg; from the magnetic equator. This allows us to model TEC values of stations located away from the magnetic equator such as Iquitos. We also present a comparison of modeled TEC values and measurements of TEC at stations away from the equator.

### **3.13 O13: Interhemispheric Flows in the Equatorial Topside Ionosphere by (student NOT in competition) Venkatraman, Sarita**

**Authors:** Sarita Venkatraman and Rod A. Heelis

**Abstract:** Latitudinal, longitudinal, and seasonal variations in the field-aligned and perpendicular flows measured at an altitude near 830 km, by the Defense Meteorological Satellite Program (DMSP) F10 satellite are examined. These profiles are studied during the nighttime (2100 MLT) for solstice periods in 1991 when the solar activity is very high. Latitude and longitude variations show the influence of F-region winds in modulating the observed field-aligned flows. At night, large downward field-aligned flows of the order 400-600 m/s are observed in the winter hemisphere and coincide in longitude with the location of previously identified adiabatic heating effects studied by Venkatraman and Heelis [1999a]. Interhemispheric flows at 2100 hrs local time are seen to extend up to apex heights of about 1000 km during times of high solar activity. Perpendicular drifts however, are relatively invariant with latitude as expected.

The ability to combine latitude profiles of the ionospheric temperature, composition, and velocities at specific longitude and local time and comparing these to the available wind data, enables us to quantify the wind influence on the topside ionosphere and its role in affecting the interhemispheric transport of plasma across the equator. An extensive database of nighttime F-region winds from Arequipa, South America, are also analyzed in the presented work. By comparing the daily variations in the topside with those seen in the F-region winds, we can uncover those changes that may be attributed directly to neutral winds.

### **3.14 O14: Comparison of ionospheric parameters derived from airglow observations and incoherent scatter radar measurements by (student in competition) Makela, Jonathan J**

**Authors:** Jonathan J. Makela Michael C. Kelley Nestor Aponte Sixto A. Gonzalez

**Abstract:** Using the Cornell AllSky Imager (CASI) located at Arecibo, observations of the 6300A and 7774A airglow lines were made. We present four nights during 1999 where we have simultaneous incoherent scatter radar (ISR) measurements of electron density. From the ISR data, we can model these two lines. From the CASI observations, we can estimate the F-region parameters nmf2 and hmf2. Two nights show good correlation between the ISR-measured and the CASI-observed parameters. Marginal success was achieved on the other two nights due to discrepancies in the measured and modeled 7774A line, suggesting that some process was contributing to this line other than radiative recombination and ion-ion recombination.

### **3.15 O15: INHOMOGENEOUS STRUCTURE OF IONOSPHERE OVER ARECIBO by (student in competition) Zhou, Qina**

**Authors:** Qina zhou; J.D. Mathews; Q.H. Zhou

**Abstract:** F region tilt structure of electron density over Arecibo is presented in the poster. The way to identify it, its characteristic, and what may causes it will also be discussed.

### **3.16 O17: Title: Ionospheric Tomography with the Global Positioning System by Tsai, Lung-Chih**

**Authors:** L.-C. Tsai, and W. H. Tsai

**Abstract:** Measuring the GPS signals and determining the path TECs from both of ground systems and a satellite receiver in Low Earth orbit can provide a powerful means for tomographic reconstruction of the ionosphere. In practice, the TEC data from a network of ground-based GPS receivers can provide detailed information on the horizontal structure; OTOH, the available occulting TEC data are sensitive to small vertical structure of approximately a few kilometers. We have implemented the SVD method and the MART algorithm to regularize the inverse problem associated with ionospheric stochastic tomography.

### **3.17 O18: The traveling ionospheric disturbances observed by GPS receivers at mid-latitudes by Saito, Akinori**

**Authors:** A. SAITO, M.C. Kelley, J.M. Makela, T. Tsugawa, Y. Otsuka, and S. Miyazaki

**Abstract:** Local time, seasonal and solar cycle dependencies of the traveling ionospheric disturbances (TIDs) were studied with the total electron content observations by GPS receivers. GEONET (GPS earth observation network) in Japan have detected TIDs since 1997. At nighttime, the south-westward propagating TIDs are dominant, and their amplitude is larger in summer than in winter. TIDs were observed in the daytime to propagate southward. The daytime TIDs have larger amplitude in the winter season. The anti-correlation between the TID activity and solar cycle was observed.

### **3.18 O19: Gravity Wave Signatures in the Ionosphere of Jupiter. by (student in competition) Matcheva, Katia**

**Authors:** K. I. Matcheva, D. F. Strobel, F. M. Flasar

**Abstract:** The electron density profiles of the ionosphere of Jupiter exhibit a system of thin layers in the region below the main electron density peak. We suggest that the observed features are signatures of propagating Gravity Waves and construct a non-linear numerical model of the ionospheric response to GW forcing. Our results show that GW with parameters inferred from the thermal structure of the neutral atmosphere can have a major impact on the plasma distribution, creating large peaks in the electron density. Wave driven electron fluxes and global implications are discussed.

### **3.19 O20: Vibrational distributions of the N<sub>2</sub><sup>+</sup>(A) and N<sub>2</sub><sup>+</sup>(B) states in the terrestrial midlatitude and auroral ionospheres by Fox, Jane L.**

**Authors:** Jane L. Fox Thomas Skinner

**Abstract:** We have modeled the vibrational distribution of the N<sub>2</sub><sup>+</sup>(A) and N<sub>2</sub><sup>+</sup>(B) states for both the midlatitude and auroral terrestrial ionospheres. Our models include transport of the N<sub>2</sub><sup>+</sup> excited state ions. For the auroral case, electron-induced fluorescence plays an important role in determining the vibrational distribution. For the sunlit ionosphere, solar fluorescence dominates at high altitudes. We compare our results to those obtained by Broadfoot [1971], Degen [1981], and Fox and Dalgarno [1985], and to the recent measurements of Morrison et al. [1999].

### **3.20 O21: Global Conductances from AMIE using POLAR UVI images by CROWLEY, GEOFF**

**Authors:** Geoff Crowley, Thomas J. Immel, Aaron J. Ridley, Delores J. Knipp, Dirk Lummerzheim, Jeff Thayer, F. Rich and Arthur D. Richmond

**Abstract:** The Assimilative Mapping of Ionospheric Electrodynamics (AMIE) procedure provides global maps of high latitude electric fields and conductances, from which the simple Joule heating (neglecting neutral wind effects) can be obtained. To determine whether these estimates are realistic, it is important to determine the accuracy of the AMIE conductances and electric fields. Historically, conductance data have been especially difficult to obtain for ingestion into AMIE, but recent POLAR UVI images have provided

conductances on a global scale that can be ingested into AMIE. This paper demonstrates the sensitivity of the conductances derived by AMIE to the inclusion of conductances inferred from UVI, magnetometers and DMSP particle data for the May 1998 storm. The AMIE runs are tuned such that the dayside ionospheric conductances compare favorably with height-integrated values derived from measurements by the Sondrestrom incoherent scatter radar. The UVI images promise to dramatically! improve the AMIE conductance and electric field distributions, and subsequently Joule heating by providing conductance estimates where no other data are available. The significant changes in AMIE conductances caused by the introduction of UVI data are described here. In addition, this paper provides the first validation of the UVI conductances by comparing them with conductances derived from DMSP particle data. Good agreement is obtained between the UVI and DMSP estimates.

### **3.21 O22: Performance of the Weimer Ionospheric Convection Model Model with Satellite Data for Space Weather Applications by Hairston, Marc**

**Authors:** M. Hairston, D. Weimer, O. Kivanc and R. Heelis

**Abstract:** One of the key questions in space weather and ionospheric modelling is the accuracy of the predictions made by the models. We compare a month's worth of cross polar cap potentials observed by the DMSP-F13 satellite in the northern hemisphere with the predicted patterns from the Weimer model using concurrent IMF observations. The results enable us to judge the performance of the model under various IMF conditions.

### **3.22 O23: Convection Electric Field Products at the JHU/APL SuperDARN Web Site by Greenwald, Raymond**

**Authors:** R. A. Greenwald, J. M. Ruohoniemi, S. G. Shepherd, and R. Barnes

**Abstract:** Many improvements have been made to the JHU/APL SuperDARN web pages (<http://superdarn.jhuapl.edu>), including real-time products (convection maps, range/beam Doppler velocity plots, and various space weather products), event study periods, and data archives from 1993 to present. Significant improvements to these web pages allow scientists easy access to SuperDARN data products and contact with collaborating scientists.

### **3.23 O24: The Polar Ionosphere under conditions of Northward IMF: Numerical Modeling and comparison with data by (student in competition) Kombiyil, Raj**

**Authors:** R.Kombiyil B.J.Watkins S.A.Maurits

**Abstract:** A time dependent three dimensional model of the polar ionosphere has been run for conditions of northward IMF over an extended period (January 23,24;1998). The model results from the F region is used to study the associated ionospheric dynamics(UT effects etc.) over a spatial region for comparison with data from the Sondrestrom ISR. These comparisons are used to validate the model for possible future space weather predicitive applications.

### **3.24 O25: Near-simulataneous POLAR and DMSP Measurements of Topside Ionospheric Field-aligned Flows at High Latitudes by (student in competition) Zeng, Wen**

**Authors:** W. Zeng, J. L. Horwitz, B. A. Stevenson, X.-Y. Wu,Y.-J. Su, P. D. Craven, F. J. Rich, and T. E. Moore

**Abstract:** Near-simultaneous observations of topside O+ parallel flows are presented for four periods of measurement by POLAR and DMSP satellites during April 1996. These observations provide a view of

wide-spread upward/downward ionospheric O+ flows over the broad polar region along extended and multiple distinct satellite tracks. We have also examined the dual altitude parameter measurements approximately 30 minutes apart for a polar cap field line, and compared them with results from a transport simulation in which a flux tube was subjected to a brief pulse of soft electron precipitation and topside transverse ion heating. The simulated density and velocity altitude profiles for approximately 20 minutes after pulse generally matched the observations.

### **3.25 O26: Whistler-mode Wave Injection Experiments in the Plasmasphere with a Radio Sounder by (student in competition) Chen, Xiangdong**

**Authors:** Vikas S. Sonwalkar, Jayashree Harikumar, Don L. Carpenter, T. F. Bell

**Abstract:** Whistler-mode wave-injection experiments with a high-latitude radio sounder offer an opportunity to greatly extend the observing power of satellites such as IMAGE (Image for Magnetopause-to-Aurora Global Exploration) when the satellite is within or near the plasmasphere or at low altitudes over the polar regions.

### **3.26 O27: The Role of Wave-Particle Interactions on Ionosphere-Magnetosphere Coupling by Barakat, Abdallah**

**Authors:** A. R. Barakat and R. W. Schunk

**Abstract:**

In the ionosphere-magnetosphere coupled system, it is generally accepted that the ionosphere supplies most of the mass/momentum, while the magnetosphere supplies most of the energy. In order to address this problem, we use a time-dependent generalized polar wind model that consists of a fluid-based component at low altitudes and a macroscopic particle-in-cell (mac-PIC) component at high altitudes. The simulation follows a magnetic flux tube that extends from  $\sim 100$  km to 8 RE altitudes as it drifts across the cusp, polar cap, auroral and subauroral regions. We investigate the relative importance of the WPI and the energetic electrons (of magnetospheric origin) on the ion outflow and temperature in the different high-latitude regions. The main conclusions of this study are as follows: (1) The interplay between the thermal ionospheric and energetic magnetospheric electrons produces a double-layer whose strength and altitude varies with time in response to the variation of the geophysical conditions; (2) The WPI influence is more pronounced on the ion temperature and progressively less important on the vertical drift,  $u(\text{H}^+)$ , and the density,  $n(\text{H}^+)$ , respectively; (3) The effects of the WPI are strongest in the cusp region; (4) In contrast, the presence of the magnetospheric electrons is the dominant factor for the evolutions of  $n(\text{H}^+)$  and  $u(\text{H}^+)$  in the polar cap; and (5) The profiles of  $n(\text{H}^+)$  and  $u(\text{H}^+)$  change more rapidly as they move from the subauroral to cusp region than as they move from the cusp to the polar cap.

### **3.27 O28: A Statistical Survey of the Effects of Solar Wind Structures on the Ionosphere and Magnetosphere by Knipp, Delores**

**Authors:** Delores J. Knipp Linda H. Krause

**Abstract:** Three types of solar wind structures are widely recognized: Ejecta, high speed solar wind, and slow solar wind flow. Richardson et al (JGR, submitted, 2000) have classified the solar wind observations for the interval 1972-1986 and compared them to the AA index. We use their classification scheme to estimate the influence these structures have on the ionosphere and magnetosphere by analyzing the Polar Cap Index, Auroral Electrojet and Dst response to these structures. We attempt to determine in some types of flows are more effective in energizing the ionosphere versus the magnetosphere.

### 3.28 O29: A fully coupled global MHD model of the magnetosphere and ionosphere by schoendorf, jackie

**Authors:** j. schoendorf k.d. siebert w.w. white

**Abstract:** We introduce a fully coupled MHD model of the global magnetosphere, ionosphere, and thermosphere from  $\tilde{80}$  km out to the solar wind. Typically, magnetospheric MHD models treat the ionosphere as a boundary condition. We describe our MHD model which includes a new self-consistent thermosphere and ionosphere.

## 4 Wednesday Evening 28 June 2000 Poster Session Titles, Mesopause Region and Below (M)

### 4.1 M01: Long-term variations of atmospheric waves observed with meteor and MF radars in Indonesia by Tsuda, Toshitaka

**Authors:** Toshitaka Tsuda, Takuji Nakamura, R. A. Vincent, I. M. Reid and Agus Nuryanto

**Abstract:** Long-term variations of ultra-fast Kelvin (U FK) waves, atmospheric tides and gravity waves in the equatorial MLT region are analyzed by using meteor winds and MF radar data collected in Indonesia in 1992-9. Semi-annual periodicity in the wave activity was recognized in a wide wave frequency range. The wave activity was conspicuously depressed in 1996-7, which suggests weak excitation of waves by convection in the troposphere.

### 4.2 M02: Initial Observations of Mesospheric Winds Using IDI Radar Measurements at the Bear Lake Observatory by studentno; changed to student-tyes (meh 6/12/00) Fish, Chad

**Authors:** F.T. Berkey G.O.L. Jones

**Abstract:** The adaptation of Imaging Doppler Interferometry to the dynasonde deployed at the Bear Lake Observatory enable the routine measurement of mesospheric dynamics. Influenced by the direction of the prevailing wind, a clear seasonal variation is seen in the mesospheric echo numbers. The techniques also provide a monitor for the amplitude of the main tidal modes as well as for studying planetary waves with periods between 2-20 days. The observations are consistent with optical measurements from Bear Lake thereby confirming the IDI characterization of the mesospheric wind field.

### 4.3 M3: Observations of PMSE Using Coherent Radar Imaging: Direct Evidence of Wave Steepening by (student in competition) Yu, Tian-You

**Authors:** Tian-You Yu, Robert D. Palmer, and Phillip B. Chilson

**Abstract:** In this work, coherent radar imaging (CRI) was implemented using the ESRAD (ESrange mst RADar) system in Kiruna, Sweden in the summer of 1998. Horizontal structures of polar mesosphere summer echoes (PMSE) are first studied with highly temporal and angular resolution using CRI. Frequency jumps, which are sudden changes in the radial velocity, were observed in several regions during this experiment. By analyzing the spectrograms and the brightness distribution estimates during two cases of frequency jumps, it was evident that the frequency jump was caused by a steepened wave structure. The existence of steepened wave is further verified using a simulation model.

### 4.4 M04: The Photolysis of Sodium Compounds in the Upper Atmosphere by (student in competition) Self, Daniel Emitt

**Authors:** Daniel E Self John M C Plane

**Abstract:** Understanding of the meteoric sodium layer has been limited by the difficulty in observing sodium compounds, compounded with the difficulties involved in simulating the chemistry in the laboratory. Until recently, only the atomic sodium was detectable by LIDAR at night and rocket missions could detect cations, whose profiles models have successfully described. But new diurnal and seasonal Na-LIDAR data have been collected at Urbana, IL, which require this laboratory-based research on the sodium compounds, to discover how the sun affects the sodium layer.

#### 4.5 M05: Analysis of Na Temperature Lidar Measurements: Calculation of Stability of the Mesopause Region by (student NOT in competition) Madine, Sean

**Authors:**

**Abstract:** Analysis of high resolution temperature profiles of the mesopause region above Fort Collins, CO (40.6 N, 105 W) for the time period from 1990 to 1999 was performed. This poster presents the results of computations of lapse rate, Brunt-Vaisala frequency and Richardson number. The time resolution of the analyzed data is 1 hour, and the height resolution is 75 meters. These calculations were performed in an attempt to identify interesting gravity wave events for further study.

#### 4.6 M06: Mesospheric Stability and Temperatures Over Utah and Ontario by (student in competition) Nelson, Karen L

**Authors:** Karen L Nelson V. Wickwar J. Herron R. Sica S. Argall

**Abstract:** The locations of Utah State's Atmospheric Lidar Observatory (ALO) and the University of Western Ontario's Purple Crow Lidar (PCL) are at similar latitudes and dissimilar longitudes, with significant orographical differences. A comparison has been made of mesospheric temperature profiles and adiabatic lapse rates from each facility and from two models, one empirical (1990 MSIS) and one theoretical (from Ray Roble), for four months in 1998. The ALO and PCL temperatures are surprisingly similar. The adiabatic lapse rates measured at each location are also similar, with small differences that can be attributed to a less stable atmosphere over the Rocky Mountains.

#### 4.7 M07: Lidar Observations of Middle Atmosphere Temperature and Fe Density During the 1999 Airborne Arctic Campaign by (student in competition) Pan, Weilin

**Authors:** Weilin Pan Chester Gardner George Papen Xinzhaio Chu

**Abstract:** In the summer of 1999, we conducted an Airborne Arctic Campaign with University of Illinois Fe Boltzmann temperature Lidar deployed in NSF NCAR Electra aircraft. With the capability of both night-time and day-time measurements, we obtained range-resolved mesospheric and lower thermospheric temperature profiles above geographic North Pole, measured temperature and Fe density over Arctic, and recorded Noctilucent Clouds (NLC) as well.

#### 4.8 M09: Rayleigh Lidar Studies of the Arctic Middle Atmosphere by (student in competition) Cutler, Laura J.

**Authors:** Laura Cutler, Dr. Richard Collins

**Abstract:** An engineering analysis of Rayleigh lidar system performance with sensitivities to operational parameters will be shown, with the main issue being that of the overlap of the laser beam divergence to the telescope FOV. A robust algorithm for density and temperature processing under a range of geophysical conditions, such as mesospheric inversion layers, will also be presented. This analysis will be using a three-year data set obtained at Poker Flat Research Range, Chatinika, Alaska.

#### 4.9 M09: Climatology from Atmospheric Lidar Observatory USU/CASS by (student in competition) Herron, Joshua

**Authors:** Josh Herron Vincent Wickwar Karen Marchant

**Abstract:** Results from the Atmospheric Lidar Observatory operated by Utah State University located in Logan, UT. The ALO system is a rayleigh scatter lidar providing temperatures between 45 to 95 km.

#### 4.10 M10: Mesospheric Temperatures Probed by Simultaneous Measurement of OH and O2 in the Nightglow by Cosby, Philip C.

**Authors:** P. C. Cosby, T. G. Slanger, D. L. Huestis, and D. E. Osterbrock

**Abstract:** The terrestrial nightglow is observed with high spectral resolution and over a wide range of intensity by the HIRES spectrometer of the Keck I telescope, during the normal course of astronomical observations. We present the initial analysis of this data set to extract rotational temperatures of a wide range of OH Meinel and O2 Atmospheric band emissions.

#### 4.11 M11: Resolving Ambiguities in Gravity Wave Propagation Directions Inherent in Satellite Observations: A Simulation Study by Brown, Jason S.

**Authors:** Jason S. Brown Michael Hickey

**Abstract:** We simulate space-based, limb viewing observations of airglow brightness fluctuations caused by atmospheric gravity wave interactions with the O2 atmospheric airglow, and we demonstrate that due to the geometry associated with such observations, the brightness fluctuations will always appear stronger for waves traveling towards the observer (satellite). The effect should be most noticeable for waves having relatively small vertical wavelengths ( $\sim 10$ km) and horizontal wavelengths of 50km or greater. Therefore, the 180 degree ambiguity in wave propagation direction associated with space-based observations may be eliminated for waves dissipating in the upper mesosphere and lower thermosphere.

#### 4.12 M12: The Numerical Simulation of Gravity Wave Packets and Their Effects on the OI 5577 Airglow by Hickey, Michael

**Authors:** Michael P. Hickey Richard L. Walterscheid Philip G. Richards

**Abstract:** The propagation of a Gaussian wave packet (comprised of as many as 2000 individual monochromatic waves) through the atmosphere is simulated using a spectral approach. Each of the constituent waves is simulated using our full-wave model. We assume a source height of 15 km. The perturbation velocities, temperature, and density are input to a 2-D, time-dependent, nonlinear chemistry model to simulate variations in minor species and the OI 5577 airglow. In addition to the fluctuating part, the response also consists of a secular part forced by wave transience and wave dissipation. We study two different wave packets and their effects on the airglow and on the O distribution.

#### 4.13 M13: Effects of Mean Winds on Gravity Wave-Driven O2 Atmospheric Airglow Fluctuations by (student NOT in competition) Hammett, Robert

**Authors:** Robert D. Hammett, Michael P. Hickey

**Abstract:** We use a full-wave dynamical model and a steady-state, linear chemistry model, to simulate gravity wave-driven airglow fluctuations for the O2 atmospheric emission. Our primary goal is to determine the effects of mean winds on the relative airglow fluctuation amplitude, and we do so by using the mean winds derived from the Horizontal Wind Model in our simulations. Calculations are performed for nighttime conditions at 18 degrees north and for summer and winter solstice. The effects of mean winds on the waves is a strong function of wave propagation speed and direction. We therefore choose four propagation directions (north, south, east and west) and a range of horizontal phase speeds (20 m/s to 100 m/s) for a single value of horizontal wavelength (80 km).

#### 4.14 M14: Relation of Intensity Perturbation and Vertical Wind Velocity of Acoustic Gravity Wave by (student in competition) Hsia, Justin

**Authors:** Justin Hsia, first author Gary Swenson, advisor Alan Liu, advisor

**Abstract:** The poster presents the first attempt to verify the relation between intensity perturbation and vertical wind velocity of acoustic gravity wave theorized by Swenson and Gardner. Intensity perturbation is measured using airglow imager, centered at OH band. Vertical wind velocity is measured using lidar. Both systems are situated at Kirkland AFB.

#### 4.15 M15: Investigation of Gravity Waves Using Starfire Data by Huang, Tai-Yin

**Authors:** Tai-Yin Huang, Michael Hickey and Sarah Stanhope

**Abstract:** We performed gravity wave studies for the mesospheric region using data collected at the Starfire Optical Range, NM in 1994 and 1995. These data exist for eight different nights (one in November, three in February and four in April ) and consist of observations of Na density, temperature, and horizontal and vertical winds measured with a Na wind/temperature lidar. A preliminary analysis of the data is presented. Contour plots of Na density, temperature and vertical winds show considerable differences at different seasons. Day to day variation is also apparent. The time average of Na density and temperature for each day show that Na density is larger in winter and the temperature is correspondingly colder except for February 2, 1995. On that day, the vertical profiles of the temperature and Na density show prominent wave-like structure and the temperature has a peak at 95 km that was not found for other nights. Variations are obtained by subtracting the mean from the data (for Na density, temperature and vertical velocity) to study the effects of gravity wave perturbations. Spectral analysis of vertical winds using a discrete Fourier transform is performed and wave characteristics are derived.

#### 4.16 M16: Directional Dependence of Gravity Wave Propagation Over Fort Collins Colorado by (student in competition) Jorgensen, Arlynda

**Authors:** A.W. Jorgensen, M.J. Taylor

**Abstract:** Data from the Fort Collins Temperature Mapper Campaign has been analyzed for directional properties. The data shows a correlation between season and direction of wave propagation.

#### 4.17 M17: Characteristic of Atmospheric Gravity Waves observed during the WAVE2000 Campaign in Japan by (student in competition) Onishi, Hisanaga

**Authors:**

H. Onishi, Y. Yamada, H. Fukunishi, M. Kubota, M. Ishii, Y. Murayama, and K. Igarashi, N. Iwagami, K. Oyama

**Abstract:** On January 2000, the WAVE2000 campaign was carried out in Kagoshima, Japan. We will report the results of altitude of the airglow emission layer estimated by ground-based triangulation and gravity wave parameters. We will also discuss the general characteristics of gravity waves observed during this campaign.

#### 4.18 M18: Observations of High Frequency Gravity Wave Spectra in the Middle Upper Stratosphere by (student in competition) Russell, Albert

**Authors:** A. T. Russell and R. J. Sica, Dept. of Physics and Astronomy, University of Western Ontario, London, Ontario, Canada

**Abstract:** The spectral analysis of density fluctuations obtained with the Purple Crow Lidar has shown that middle upper stratospheric temporal spectra follow the expected -1.5 to -2.0 power law to frequencies of approximately 1/(15 min). At higher frequencies, the shape of the spectrum is much more variable with strong quasi-monochromatic features appearing intermittently on certain nights. These higher frequency features have been attributed to nonlinear wave interactions and suggest that estimates of middle upper stratospheric gravity wave activity, energy dissipation, and eddy diffusion values may be much larger and more variable than previously assumed.

#### **4.19 M19: Automation and Animation Techniques for Investigation of Gravity Waves in the Infrared Airglow by (student NOT in competition) Krueger, Todd M.**

**Authors:** Todd M. Krueger Katelyn N. Allers Delbert R. Friesen Lois M. Kieffaber

**Abstract:** A new automation program designed to control our CCD imager takes images at a constant time rate, eliminating the need for a human operator. In addition to providing ground-based support for the TIMED satellite, the new program is useful for making time-lapse movies.

#### **4.20 M20: Simulation of 3-day Kelvin wave influence on Greenline, O<sub>2</sub> Atmospheric, and OH Meinel band emissions in the MLT region. by (student in competition) Lichstein, Gilbert S.**

**Authors:** G. S. Lichstein J. M. Forbes M. Angelats i Coll

**Abstract:** Evidence now exists for the presence of a 3-day ultra-fast Kelvin wave in the mesosphere and lower thermosphere. Herein we report on the airglow signatures consistent with this oscillation using an extension of an existing one-dimensional finite element dynamical-chemical model, which now calculates O<sub>2</sub> atmospheric band and OH(9-3) emission rates in addition to the oxygen greenline. The resulting peak-to-peak height-integrated emission rate variations for this Kelvin wave during July are of order 15-20% for all three emissions.

#### **4.21 M21: Dynamical processes related to the atomic oxygen springtime transition by Liu, Han-Li**

**Authors:** Han-Li Liu and Ray Roble

**Abstract:** Both ground based and satellite observations have shown a "springtime transition" in the night-time oxygen airglow emission rates with a sharp net decrease over several days around spring equinox. This transition is studied using the NCAR/TIME-GCM year-run simulations. Model results show a close relation between this transition and the residual circulation change in the mesosphere region during equinox, which is in turn determined by gravity wave forcing. Variabilities due to planetary waves and implications on the stability of equinoctial mesosphere will be discussed.

#### **4.22 M22: Uranus: Gravity waves, the momentum budget, and adiabatic cooling. by Young, Leslie A.**

**Authors:** Leslie A. Young

**Abstract:** The temperature of the Uranian atmosphere at 20 microbar varies by 50 K on the timescale of decades. Between 1983 and 1998, it has decreased at a rate of 3 K/year – far too rapidly to be caused solely by radiative cooling by methane and other hydrocarbons. One possible explanation is adiabatic cooling, driven by momentum deposition of breaking gravity waves (with associated adiabatic heating elsewhere). Gravity waves with vertical wavelengths near 2.5 km, which have been detected in the Uranian upper atmosphere, should be capable of forcing the required winds.

#### 4.23 M23: A Mechanistic Wave-Mean Flow Interaction Model - First Results by Meyer, Christian

**Authors:** C.K. Meyer (NCAR, HAO) M.E. Hagan (NCAR, HAO)

**Abstract:** A time dependent, quasi non-linear global scale model of wave-mean flow interactions is being developed at NCAR-HAO for use by the PSMOS and CEDAR communities. Initial results of interactions between planetary waves and tides and the zonal mean background atmosphere are presented and contrasted with observations and modeling of the diurnal tide quasi 2-day wave.

#### 4.24 M24: Intradiurnal Oscillations in the Mesosphere and Lower Thermosphere by (student in competition) Sharma, Niranjana

**Authors:** Niranjana R. Sharma Jeffrey M. Forbes

**Abstract:** Intradiurnal oscillations with periods between about 6 and 11 hours have been observed by various researchers in the mesosphere and lower thermosphere (MLT) over South Pole. Oscillations in the wind field have been interpreted as gravitational normal modes, or Lamb Waves, and those in temperature and airglow intensity as zonally symmetric tides. In the present work, the Global Scale Wave Model is utilized to simulate the global structures of these oscillations, and to evaluate the effects of mean winds on their accessibility to the polar MLT regions. The seasonal dependence of the zonal mean winds for wave propagation is found to produce significant reductions in the amplitudes of intradiurnal oscillations over the polar regions during summer months. This comes about through coupling into other modes which modify the total response to accommodate distortion by the mean wind field. In addition, much smaller wind amplitudes are found for eastward vs. westward propagating waves over the polar regions. Both of these numerical results are in agreement with the observations over South Pole.

#### 4.25 M25: Migrating and Nonmigrating Semidiurnal Tide Components From Combined Space-based and Ground-based Measurements by (student in competition) Cierpik, Kim

**Authors:** Kim M. Cierpik, Jeffrey M. Forbes, Scott E. Palo, A. Fahrutdinova, C. Jacobi, A. Manson, S. Miyahara, N.J. Mitchell, Y. Portnyagin

**Abstract:** The purpose of this investigation is to use combined ground-based and space-based measurements of winds to derive the migrating and nonmigrating semidiurnal tidal components in the mesosphere and lower thermosphere between 50-55N. To better understand the aliasing and sampling issues, a mock data set is formed by sampling the Kyushu University GCM output from both the ground and satellite perspectives, and analyzed in the same manner as the actual measurements. Comparisons with full analysis of the GCM provides insight into uncertainties connected with the true measurement analysis. Particular attention is devoted to extracting the month-to-month variability of the tidal components and their longitudinal structure.

#### 4.26 M26: TIME-GCM simulations of the diurnal variation of lower thermospheric nitric oxide observed by HALOE by Marsh, Dan

**Authors:** Dan Marsh and Ray Roble High Altitude Observatory, National Center for Atmospheric Research

**Abstract:** The UARS Halogen Occultation Experiment (HALOE) uses solar occultation to measure nitric oxide (NO) up to an altitude of 130 km. Significant differences exist between sunrise and sunset HALOE observations. TIME-GCM simulations show that these differences are consistent with perturbations induced by the diurnal tide. Clear tidal signatures are present that are the result of vertical motions in a background atmosphere that has a steep vertical gradient in NO. In addition, the observed seasonal and interannual NO variability appears to be linked to tidal variability.

#### 4.27 M27: Nitrous Oxide(N<sub>2</sub>O) production in sprites by (student in competition) Moudry, Dana

**Authors:** D.R. Moudry, W.R. Simpson and H.C. Stenbaek-Nielsen

**Abstract:** Nitrous Oxide(N<sub>2</sub>O) is an important greenhouse gas as well as a trace gas used to study atmospheric dynamics. Currently most sources of N<sub>2</sub>O are believed to be biogenic and anthropogenic. We propose sprites as a mesospheric source of N<sub>2</sub>O. While this source is very small compared to the total (1 Gg: 10 Tg), the proposed mesospheric N<sub>2</sub>O density perturbation due to sprites above thunderstorms should be visible by limb scanning satellites. In addition, the N<sub>2</sub>O chemistry could be indicative of further chemistry from highly vibrationally excited molecules.

#### 4.28 M28: Statistical Parameters of Lightning in Sprite-Associated Storms. by (student in competition) So Sabbas, Fernanda T.

**Authors:** So Sabbas<sup>1</sup>, F. T.; Pinto Jr.<sup>2</sup>, O.; Mendes Jr.<sup>2</sup>, O.; Taylor<sup>3</sup>, M. J. 1 - University of Alaska, USA 2 - INPE, Brazil 3 - Utah State University, USA

**Abstract:** The relationship between sprites and lightning in their associated thunderstorms was investigated for a seven-day period (700 events) during the Sprites96 Campaign. Sprites occurred over storms possessing 7-17% +CG flashes, indicating that a high percentage of +CG flashes is not necessary for sprite occurrence. The average of the peak currents for sprite associated +CG flashes was higher than the one for all +CGs of the storm. However, the maximum in the sprite associated peak current distribution was at 40-50 kA. Approximately 6% of the sprites were associated with +CGs of less than 20 kA, lower values than previously reported, and 10% were associated with negative lightning.

#### 4.29 M29: Estimation of the Energies of Electrons Inducing Elves Observed above Japan in Winter by (student in competition) Miyasato, Rina

**Authors:** Rina Miyasato, Yukihiro Takahashi, Akihiro Uchida, Masaaki Sera, Hiroshi Fukunishi

**Abstract:** We carried out optical observations of sprites and elves at Maebashi in Japan from December 1999 to February 2000 with two multi-anode array photometers(MAP) and an image intensified CCD camera and other optical instruments. The two MAP instruments were equipped with filters, red(380-500 nm)and blue(560-800 nm), respectively. We succeeded in capturing spectral data for 4 events of elves during this campaign. Using these spectral data, we calculated the energies of electrons inducing elves, and we compared these results with the characteristics of elves observed in Colorado,USA.

#### 4.30 M30: A Study of 19.5 GHz Brightness Temperature over Taiwan Area by (student NOT in competition) Shih, Shun-Peng

**Authors:** Shun-Peng Shih Yen-Hsyang Chu

**Abstract:** Using a single-frequency ground-based microwave radiometer with steerable horn antenna at frequency 19.5 GHz, we measure sky radiometric temperature over Taiwan area during the period from May 1997 to September 1999. Statistics indicates that for more than 80% of the time in the absence of surface precipitation the brightness temperature is above 27 K. Multi-zenith angle observations show that the median brightness temperature increases with zenith angle from about 30 K at zenith to about 128 K at 80X off-zenith angle. The opacity  $t$  of atmosphere is also observed. We found that basically the dependence of opacity  $t(q)$  on zenith angle  $q$  follows perfectly the secant law, namely,  $t(q)=t_0 \sec(q)$  ( $t_0$  is zenith opacity), if the zenith angle is less than 70X.

**4.31 M31: Anomalous Behavior of Precipitation Doppler Spectrum Associated With Strong Vertical Air Motion by (student NOT in competition) Su, Ching-Lun**

**Authors:** Ching-Lun Su Meng-Yuan Chen Yen-Hsyang Chu

**Abstract:**

## 5 Tuesday Evening 27 June 2000 Poster Session Titles, Thermosphere and Regions Aloft (T)

### 5.1 T01: Estimates of Terdiurnal Oscillations at Sondre Stromfjord by Azeem, Irfan

**Authors:** S. M. Irfan Azeem

**Abstract:** Neutral winds derived from the Sondre Stromfjord incoherent scatter radar data are analyzed to investigate the structure of terdiurnal oscillations in the 90-130 km altitude interval. Measurements obtained during the core period of Lower Thermosphere Coupling Study (LTCS) campaigns have been used here to investigate the variability of terdiurnal signal seen in the periodograms of Sondrestrom neutral winds. Correlations with the diurnal and semidiurnal oscillations (estimated from the Sondrestrom data) are presented.

### 5.2 T02: COMPARISON OF THE AURORAL E REGION NEUTRAL WINDS DERIVED BY THE EISCAT RADAR AND PREDICTED BY NCAR TIME-GCM. by Nozawa, Satonori

**Authors:** S. Nozawa, A.D. Richmond, R. Roble, and H.-L. Liu

**Abstract:** A comparison study of the auroral E region neutral wind is conducted using the European Incoherent Scatter (EISCAT) radar observations and Thermosphere-Ionosphere-mesosphere-electrodynamics general circulation model (TIME-GCM) predictions. Daily mean wind as well as diurnal and semidiurnal tidal winds are compared for three seasons such as summer, equinox and winter between 95 and 120 km. Fairly good agreement is found in an altitude profile of the mean zonal wind between the EISCAT observation and the TIME-GCM prediction for summer, which blows westward in the mesosphere and eastward in the lower thermosphere in the TIME-GCM predictions. This confirms the gravity wave (GW) plays a role in the dynamics in the upper mesosphere and lower thermosphere, and its parameterization used in the TIME-GCM is well developed.

### 5.3 T03: Neutral winds in the lower thermosphere observed by WINDII during the April 4-5th, 1993 and February 1994 storms by Zhang, Shengpan

**Authors:** Shengpan P. Zhang Gordon G. Shepherd

**Abstract:** Neutral winds in the lower thermosphere between 90 and 250 km during geomagnetic storms in April 1993 and February 1994 were observed by WINDII on UARS through the daytime green emission. Wind speed increases to 700 m/s at 180 km in the polar regions, and winds in geomagnetic and local time coordinates show the familiar two-cell pattern which penetrates down to 130 km. During the February 1994 storm, winds at 40S are much stronger than at 40N. The effects of the storms on the green emission rate at different altitudes and latitudes are also observed.

### 5.4 T04: Thermospheric Vertical Winds at the Auroral Oval/Polar Cap Boundary by (student in competition) Krynicki, Matthew P.

**Authors:** Matthew P. Krynicki, Mark Conde, Dirk Lummerzheim, Roger W. Smith, Mamoru Ishii

**Abstract:** High latitude thermospheric vertical wind studies in the past have identified a correlation between the direction of the vertical wind observed and the observation site's location relative to the auroral oval. Upward winds have been observed when poleward of the auroral oval, and downward winds when equatorward. Vertical wind time series obtained at Inuvik, NWT, Canada by Fabry-Perot interferometer observations of the Doppler-shifted 630 nm atomic oxygen emission have been examined, using POLAR spacecraft UVI images to identify the location of the auroral oval. The results generally confirm this correlation.

### 5.5 T05: Verifying Thermospheric Composition Effects due to Vertical Winds by (student in competition) Krynicki, Matthew P.

**Authors:**

Matthew P. Krynicki, Dirk Lummerzheim, Mark Conde, Roger W. Smith, Mamoru Ishii

**Abstract:** In an attempt to verify the possible depletion of atomic oxygen relative to molecular nitrogen,  $[O]/[N_2]$ , in the upper thermosphere due to large magnitude upward vertical winds, Fabry-Perot interferometer observations of the Doppler-shifted 630 nm atomic oxygen emission were gathered at Inuvik, NWT, Canada in conjunction with POLAR spacecraft UVI images. Upon identification of large magnitude upwellings in the vertical wind time series, actual 135.6 nm atomic oxygen UVI images are compared with artificial 135.6 nm images generated from flux and characteristic energy data and UVI calibration information. Discrepancies between actual and artificially-generated 135.6 images before and after upward wind events may indicate depletions in  $[O]/[N_2]$  in the upper thermosphere.

### 5.6 T06: SWIFT - ITCI: Space Weather Ionospheric Forecasting Tools an Ionosonde Thermospheric Composition Index by Wright, John William

**Authors:** J W Wright and R O Conkright National Geophysical Data Center, NOAA, Boulder Colorado, 80301 USA

**Abstract:** We address the need for an easily observable indicator of thermospheric state, and particularly, one sensitive to the neutral concentration ratio,  $[O]/[N_2]$ . There is a firm basis to expect that the sunrise increase of foF2 might provide an index for  $[O]/[N_2]$ . We present the global morphology of an index defined from the rate of change of foF2\*FOF2 with  $\cos(\text{solar zenith angle})$  after normalization by the F10.7 solar flux. It displays many known features of thermospheric  $[O]/[N_2]$ , including seasonal and geographic variability according to ESRO4 satellite data and the MSIS-90 model, and (in an example) magnetic storm dependences.

### 5.7 T07: Fabry-Perot Observations of the Hydrogen Geocorona by (student in competition) Mierkiewicz, Edwin, J.

**Authors:** E. Mierkiewicz F. Roesler S. Nossal

**Abstract:** A new series of observations is underway to explore the physical processes which govern the abundance and transport of atomic hydrogen in the earth's exosphere. Ground-based observations of hydrogen's solar excited Balmer-alpha emission line yield important information regarding the density, temperature, and kinetics of the emitting gas. Large gains afforded by the technique of Fabry-Perot CCD annular summing spectroscopy make this new set of observations possible, including the first detailed observations of the much fainter Balmer-beta line. Early results will be presented.

### 5.8 T08: Determination of geocoronal H-alpha intensities and upper atmospheric hydrogen densities from WHAM FP observations. by Nossal, Susan

**Authors:** S. Nossal, F.L. Roesler, R.J. Reynolds, J. Bishop, M. Haffner, S. Tufte, N. Haussen

**Abstract:** The Wisconsin H-alpha Mapper (WHAM) Fabry-Perot has acquired an extensive body of high signal-to-noise, consistently calibrated geocoronal Balmer-alpha emission data. Inter-comparison of WHAM data taken over a year and comparisons with past CHARM campaign data indicate a high level of stability in the measurements. Modeling improvements and resolution of model/data discrepancies by Bishop, along with the high signal-to-noise of the WHAM data and the multiple viewing geometries of the observations have made it possible for us to extract a "best fit" hydrogen density profile.

## Index

- Kerr, Robert B., 8
- Abdu, Mangalathayil A., 12  
Azeem, Irfan, 27
- Barakat, Abdallah, 17  
Bishop, Rebecca, 11  
Breese, Justin, 8  
Brown, Jason S., 21
- Chen, Xiangdong, 17  
Cierpik, Kim, 24  
Cosby, Philip C., 21  
CROWLEY, GEOFF, 15  
Cutler, Laura J., 20
- Duck, Thomas J., 8  
Dyrud, Lars, 11
- Ecklund, Warner L., 9
- Fish, Chad, 19  
Fox, Jane L., 15
- Greenwald, Raymond, 16
- Hairston, Marc, 16  
Hammett, Robert, 21  
Hei, Matthew A., 13  
Heinselmann, Craig, 6  
Herron, Joshua, 20  
Hickey, Michael, 21  
Hsia, Justin, 22  
Huang, Tai-Yin, 22
- Jackel, Brian J, 6  
Janches, Diego, 11  
Jorgensen, Arlynda, 22
- Kafkalidis, Julie F., 10  
Knipp, Delores, 17  
Kombiyil, Raj, 16  
Krueger, Todd M., 23  
Krynicky, Matthew P., 27, 28
- Lichstein, Gilbert S., 23  
Liu, Han-Li, 23
- Madine, Sean, 20  
Makela, Jonathan J, 14  
Marsh, Dan, 24  
Matcheva, Katia, 15  
McQuerry, Shawn, 9
- Meyer, Christian, 24  
Mierkiewicz, Edwin, J., 28  
Miyasato, Rina, 25  
Moudry, Dana, 25
- Nelson, Karen L, 20  
Nossal, Susan, 28  
Nozawa, Satonori, 27
- Onishi, Hisanaga, 22
- Palo, Scott, 9  
Pan, Weilin, 20  
Paznukhov, Vadym, 6
- Rasmussen, Beatrice K., 13  
Richards, Phil, 12  
Ruohoniemi, Michael, 6  
Russell, Albert, 22
- So Sabbas, Fernanda T., 25  
Saito, Akinori, 15  
schoendorf, jackie, 18  
Self, Daniel Emmitt, 19  
Semeter, Joshua, 9  
Sharma, Niranjana, 24  
Shepherd, Simon, 6  
Shih, Shun-Peng, 25  
Sipler, Dwight, 8  
Su, Ching-Lun, 26  
Suzuki, Nobuhiro, 11
- Tsai, Lung-Chih, 14  
Tsuda, Toshitaka, 19
- Valladares, Cesar E., 13  
Venkatraman, Sarita, 14  
Viereck, Rodney, 10  
Vincent, Robert A., 12
- Wang, Chien-Ya, 12  
Woodman, Ronald F., 10  
Wright, John William, 28
- Young, Leslie A., 23  
Yu, Tian-You, 19
- ZAITZEV, Alexander, 7  
Zeng, Wen, 16  
Zhang, Shengpan, 27  
Zhou, Qina, 14